

Growth and remodeling in the pulmonary autograft: computational evaluation using kinematic growth models and constrained mixture theory

Julie Vastmans¹; Lauranne Maes¹; Mathias Peirlinck^{2,3}; Emma Vanderveken⁴;
Filip Rega⁴; Ellen Kuhl²; Nele Famaey¹

1. Biomechanics Section, Mechanical Engineering Department, KU Leuven, Leuven, Belgium
2. Department of Mechanical Engineering, Stanford University, Stanford, CA, USA
3. IBiTech-bioMMeda, Department of Electronics and Information Systems, Ghent University, Gent, Belgium
4. Department of Cardiovascular Sciences, KU Leuven, Leuven, Belgium

Abstract

Computational investigations of how soft tissues grow and remodel are gaining more and more interest and several growth and remodeling theories have been developed. Roughly, two main groups of theories for soft tissues can be distinguished: kinematic-based growth theory and theories based on constrained mixture theory. Our goal was to apply these two theories on the same experimental data. Within the experiment, a pulmonary artery was exposed to systemic conditions. The change in diameter was followed-up over time. A mechanical and microstructural analysis of native pulmonary artery and pulmonary autograft was conducted. Whereas the kinematic-based growth theory is able to accurately capture the growth of the tissue, it does not account for the mechanobiological processes causing this growth. The constrained mixture theory takes into account the mechanobiological processes including removal, deposition and adaptation of all structural constituents, allowing us to simulate a changing microstructure and mechanical behavior.

1 Introduction

The domain of *in vivo* and *in vitro* testing is currently expanding to include *in silico* testing as well, since computational models are increasingly used to evaluate hypotheses and assess medical treatments. These computational modeling will become even more important now that regulatory agencies accept them as part of the regulatory process [1].

Mechanical behavior of soft tissues can be classified based on the timeframe of interest. On the one hand, there is the instantaneous behavior of soft tissues. On the other hand,

the long term behavior, meaning how the mechanical behavior changes over time in response to a (possibly changed) stimulus is relevant over a longer timeframe. When it comes to modeling the long-term biomechanical behavior of soft tissues, two main theories can be distinguished. On the one hand, there is kinematic-based growth, following from the publication of Rodriguez in 1994 [2]. On the other hand, theories using the constrained mixture theory emerged, starting with Humphrey *et al.* in 2002 [3]. These constrained mixture theories can either be rate-based (*e.g.* [4]) or follow an integral approach [5]. In the former, the main focus lies on the evolving reference configuration, whereas in the latter the strain energy density function of the tissue is given as $\Psi = \sum \Psi^k$ for all timepoints in the growth and remodeling process [6, 7]. Recently, a homogenized version of the latter type emerged [8]. Additionally, Latorre acknowledged the complementarity of kinematic-based growth and constrained mixture theory [9]. Below, the two main types of growth theories are shortly described.

Kinematic-based growth multiplicatively decomposes the deformation gradient \mathbf{F} into an elastic deformation gradient \mathbf{F}_{el} and a growth deformation gradient \mathbf{F}_g . The evolution equation of the growth deformation gradient is determined constitutively and can depend on a biomechanical or biophysical state (*e.g.* concentration of a protein [10]) or on the stretch or stress that the tissue experiences [11]. These models have been successfully used to model growth in the carotid artery [11], skin growth [12], dilated cardiomyopathy [13] and even atrophy in the brain [10].

The constrained mixture theory attempts to incorporate mechanobiological information by describing soft tissues as a mixture of constituents with their own turnover rate, mechanical properties and stress-free geometry, whilst being constrained to move together. This has mainly been used in arterial tissue [14, 15].

Both theories have their advantages and disadvantages. Kinematic-based growth is conceptually simple and computationally convenient, whereas the more involved and computationally expensive constrained mixture theory represents the physiological processes more closely [16]. More background information on the different models, their uses and their advantages and disadvantages, can be found in several review papers [6, 9, 17]. However, to the authors' knowledge, both theories have not yet been compared one-on-one to assess their capability to provide a computational prognosis on the evolving biomechanical behavior of the same experimental dataset. Therefore, the goal of this paper is to numerically represent the experimental data of the simplified Ross procedure taken from [18], using both approaches and evaluate their performance.

2 Materials and Methods

First, the used experimental data and the constitutive behavior of arterial tissue are briefly recapitulated. Next, the used kinematic growth theory and its implementations are outlined, followed by the constrained mixture theory. Finally, this section concludes

by giving the workflow of the virtual experiments that are used to compare the computational models to the experiments.

2.1 Experimental data

The experimental data used here is taken from [18]. Briefly, within this study, eight sheep received an unreinforced pulmonary interposition graft in aortic position, and nine sheep received a similar interposition graft reinforced with a macroporous mesh. During surgery, the aortic pressures and the imposed graft prestretch were measured and given in Table 1. Within this computational study, only the unreinforced group is used. From these eight sheep, two died during follow-up.

Follow-up after surgery consisted of three MRIs (at day four, month two and month six) and after six months the sheep were sacrificed. The relevant tissues, *i.e.* native aorta, native pulmonary artery and (un)reinforced pulmonary autograft were subjected to mechanical and histological analysis, leading to stress-stretch curves demonstrating the mechanical behavior of the different tissues and fractions of the different constituents present in the different arterial tissue types.

2.2 Constitutive behavior

Both kinematic-based growth and constrained mixture theory need to be treated within the framework of nonlinear continuum mechanics and require a constitutive description of the normal arterial behavior.

The instantaneous mechanical response of the artery is described according to the following strain energy density function

$$\Psi(\mathbf{C}) = \Psi_{vol}(\mathbf{C}) + \Psi_{iso}(\bar{I}_1) + \sum_{i=4,6} \Psi_{aniso}(\bar{I}_1, \bar{I}_i), \quad (1)$$

which represents the artery as a matrix material in which two fiber families are embedded. These fiber families are symmetrically oriented around the longitudinal direction of the artery. In this equation, the different terms can be calculated as

$$\begin{aligned} \Psi_{vol}(\mathbf{C}) &= K(J - 1)^2, \\ \Psi_{iso}(\bar{I}_1) &= C_{10}(\bar{I}_1 - 3), \\ \Psi_{aniso}(\bar{I}_i) &= \frac{k_1}{2k_2} \exp(k_2(\kappa\bar{I}_1 - (1 - 3\kappa)\bar{I}_i - 1)^2 - 1), \end{aligned} \quad (2)$$

where $\mathbf{C} = \mathbf{F}^T \mathbf{F}$ is the right Cauchy-Green strain tensor and $J = \det(\mathbf{F})$. Parameter C_{10} expresses the isotropic stiffness of the matrix material. The stiffness of the fibers is expressed by parameter k_1 . Parameter k_2 relates to the nonlinearity of the material. The dispersion in fiber direction is represented by κ [19]. Finally, the 4th and 6th invariant can be calculated as $\bar{I}_{4,6} = \bar{\mathbf{C}} : \mathbf{M}_i \otimes \mathbf{M}_i$ with \mathbf{M}_i the undeformed fiber vector for each

fiber family. These undeformed fiber vectors are expressed using the mean fiber angle α . The bulk modulus K is determined as $K = \frac{4C_{10}(1+\nu)}{3(1-2\nu)}$, with ν being the Poisson ratio. The artery is assumed to be quasi-incompressible with a Poisson ratio of 0.49. More information on this constitutive model can be found in [19].

Based on the strain energy density function (SEDF), the second Piola-Kirchhoff stress \mathbf{S} and Cauchy stress $\boldsymbol{\sigma}$ can be calculated as

$$\begin{aligned}\mathbf{S} &= 2 \frac{\partial \Psi}{\partial \mathbf{C}} \\ \boldsymbol{\sigma} &= \frac{1}{J} \mathbf{F} \mathbf{S} \mathbf{F}^T = \frac{1}{J} \frac{\partial \Psi}{\partial \mathbf{F}} \mathbf{F}^T.\end{aligned}\quad (3)$$

When implementing a material model in an implicit finite element solver (*i.e.* Abaqus Standard 2017 (Dassault Systèmes, Providence, RI, USA)), the tangent stiffness tensor needs to be provided as well.

This can be calculated in two ways. First,

$$\begin{aligned}\mathbb{C}_{IJKL} &= 2 \frac{\partial S_{IJ}}{\partial C_{KL}} \\ \mathbb{c}_{ijkl} &= \frac{1}{J} \mathbb{C}_{IJKL} F_{iI} F_{jJ} F_{kK} F_{lL} \\ \mathbb{c}_{ijkl}^{Abaqus} &= \mathbb{c}_{ijkl} + \frac{1}{2} [\delta_{ik} \sigma_{jl} + \delta_{il} \sigma_{jk} + \delta_{jk} \sigma_{il} + \delta_{jl} \sigma_{ik}].\end{aligned}\quad (4)$$

The second method to derive the tangent stiffness tensor for Abaqus is

$$\mathbb{c}_{ijkl}^{Abaqus} = \sigma_{ij} \delta_{kl} + \frac{1}{2} \left(\frac{\partial \sigma_{ij}}{\partial F_{ka}} F_{la} + \frac{\partial \sigma_{ij}}{\partial F_{la}} F_{ka} \right).\quad (5)$$

More details on the above expressions, how they are related and how to implement these can be found in [20, 21].

2.3 Kinematic growth approach

The first approach that is followed to simulate growth and remodeling is based on the kinematic growth theory. Kinematic growth (KG) theory assumes that the total deformation gradient \mathbf{F} can be multiplicatively decomposed into an elastic deformation gradient \mathbf{F}_{el} and a growth deformation gradient \mathbf{F}_g as $\mathbf{F} = \mathbf{F}_{el} \mathbf{F}_g$, visually represented in Figure 1 [2]. The volumetric change due to growth can be calculated as $\det(\mathbf{F}_g) = \theta$.

The growth deformation gradient is defined constitutively, similar to Saez *et al.* [11] as

$$\mathbf{F}_g = \mathbf{I} + (\theta - 1) \mathbf{n} \otimes \mathbf{n},\quad (6)$$

with \mathbf{n} the direction of growth which corresponds to the circumferential direction.

The evolution of the growth multiplier θ is defined as

$$\dot{\theta} = k(\theta)\phi(\lambda_{el}), \quad (7)$$

if $\lambda_{max} > \lambda_{el} > \lambda_{hom} + \varepsilon$, with

$$k(\theta) = \frac{1}{\tau_k} \frac{\theta_{max} - \theta}{\theta_{max} - 1} \quad (8)$$

$$\phi = \lambda_{el} - \lambda_{hom} \quad (9)$$

[11].

The function $k(\theta)$ limits the growth that can occur to avoid unlimited growth. Parameter τ_k represents the adaptation speed and parameter θ_{max} expresses the maximally allowed growth. The function $\phi(\lambda_{el})$ provides the growth criterion. The elastic stretch λ_{el} is chosen as the stretch felt by the collagen fibers $\lambda_{el} = (\mathbf{M} \cdot (\mathbf{C}_{el}\mathbf{M}))^{1/2}$ with \mathbf{M} the undeformed fiber direction. λ_{hom} is chosen as the stretch felt by the collagen fibers in homeostatic condition. Consequently, growth starts when an elastic stretch higher than the stretch under homeostatic conditions is reached. However, to allow for a region of stretch in which no growth occurs rather than at one specific stretch value, a threshold of $\varepsilon = 0.05$ is included before allowing growth. This region of stretch is justified by the range of stretches that the fibers feel throughout the cardiac cycle. When the collagen fibers get stretched further than λ_{max} or when they experience a stretch lower than their homeostatic stretch, no growth occurs. The condition of no growth occurring when a stretch higher than λ_{max} is reached as well as the condition of the region around the homeostatic stretch value are added to the original constitutive description of [11]. The evolution of the growth multiplier is integrated over time using an Euler backward scheme, similar as [11].

The calculated elastic deformation tensor \mathbf{F}_{el} is then used to determine the Cauchy stress as

$$\begin{aligned} \mathbf{S}_g &= 2 \frac{\partial \Psi(\mathbf{C}_{el})}{\partial \mathbf{C}_{el}} \\ \boldsymbol{\sigma} &= \frac{1}{J_{el}} \mathbf{F}_{el} \mathbf{S}_g \mathbf{F}_{el}^T. \end{aligned} \quad (10)$$

In the above equation, the second Piola Kirchhoff stress is expressed in the intermediate configuration (see Figure 1). Starting from equation 4 and knowing that the second Piola-Kirchhoff stress also depends on the growth deformation tensor, the stiffness tensor results in

$$\begin{aligned} \mathbb{C}_{abcd} &= 2 \frac{\partial S_{ab}(C, F_g)}{\partial C_{cd}} \\ &= 2 \frac{\partial S_{ab}}{\partial C_{cd}} \Big|_{F_{g,ef}} + 2 \frac{\partial S_{ab}}{\partial F_{g,ef}} \frac{\partial F_{g,ef}}{\partial C_{cd}}. \end{aligned} \quad (11)$$

Since θ is the only parameter within \mathbf{F}_g that depends on \mathbf{C} , the above equation becomes

$$\begin{aligned}\mathbb{C}_{abcd} &= 2 \frac{\partial S_{ab}}{\partial C_{cd}} \Big|_{F_{g,ef}} + 2 \frac{\partial S_{ab}}{\partial \theta} \frac{\partial \theta}{\partial C_{cd}} \\ &= \mathbb{C}_{el,abcd} + \mathbb{C}_{g,abcd}.\end{aligned}\quad (12)$$

2.4 Constrained mixture approach

The second type of growth and remodeling models that is implemented is based on the non-homogenized version of the constrained mixture theory (CMT). This theory assumes that the tissue is composed out of different constituents which have their own mechanical properties, natural (*i.e.* stress-free) configuration and turnover rate, but are constrained to move together [3]. Figure 2 visualizes the different configurations present within this approach. Valentín *et al.* proposed a finite element implementation of this theory [15], which we modified slightly, implemented in a user defined material subroutine and tested on a simplified case in [14].

Here, we assume that the relevant constituents are elastin and collagen (The effect of including smooth muscle cells is described in [22]). Consequently, the total elastic stored energy can be calculated as

$$\begin{aligned}\Psi^{total}(s) &= \Psi^{vol}(s) + \frac{\rho^{ela}}{\rho(s)}(s) \hat{\Psi}^{ela}(\bar{\mathbf{C}}^{ela}(s)) + \sum_{\tau} \left(\frac{\rho^{coll}(s, \tau)}{\rho(s)} \hat{\Psi}^{coll}(\bar{\mathbf{C}}^{coll}(s, \tau)) \right) \\ \hat{\Psi}^{ela} &= C_{10}(\bar{I}_1^{ela} - 3), \\ \hat{\Psi}_i^{coll} &= \frac{k_1}{2k_2} \exp(k_2(\kappa \bar{I}_1^{coll} - (1 - 3\kappa)\bar{I}_i^{coll} - 1)^2 - 1),\end{aligned}\quad (13)$$

in which the elastic stored energy for each constituent depends on the constituent specific deformation $\bar{\mathbf{F}}^\alpha$, schematically shown in Figure 2, since $\bar{\mathbf{C}}^\alpha = \bar{\mathbf{F}}^{\alpha,T} \bar{\mathbf{F}}^\alpha$ for $\alpha = (elastin, collagen)$. The constituent specific deformation at a specific timepoint s is calculated as $\bar{\mathbf{F}}^\alpha = \bar{\mathbf{F}}(s) \bar{\mathbf{F}}(\tau)^{-1} \mathbf{G}^\alpha$, with τ the timepoint at which the constituent was deposited. The elastin deposition stretch tensor $\mathbf{G}^{elastin}$ is calculated using an approach similar to [23, 24]. Collagen is assumed to be deposited with a constant prestretch g^{coll} of 1.1 in the fiber direction (similar to [8]), leading to a deposition stretch tensor for collagen equal to

$$\mathbf{G}^{collagen} = g^{coll} \mathbf{M} \otimes \mathbf{M} + \frac{1}{\sqrt{g^{coll}(\mathbf{I} - \mathbf{M} \otimes \mathbf{M})}} \quad (14)$$

Also, $\rho(s)$ expresses the total density at timepoint s . Elastin is assumed to have no degradation or production over the considered time frame, resulting in a constant ρ^{ela} . This assumption is justified as elastin is mostly formed during early development and has a half-life of decades [25]. Collagen on the other hand can degrade and be produced

at every timepoint. The total amount of collagen is calculated by summing over all previously deposited cohorts of collagen that are still present at that timepoint as

$$\rho^{coll}(s) = \sum_{\tau} \rho^{coll}(s, \tau) = \sum_{\tau} m^{coll}(\tau) q^{coll}(s, \tau) \Delta\tau \quad (15)$$

where $m^{coll}(\tau)$ gives the rate of collagen production at timepoint τ . The fraction of collagen that was deposited at timepoint τ and survives up until timepoint s is given by $q^{coll}(s, \tau)$. Both the production rate and degradation rate depend on a mechanical stimulus δ .

The production term is calculated as

$$m^{coll}(\tau) = m^0 \Gamma(K_{\sigma}, \delta) \quad (16)$$

where m^0 is the rate of production under homeostatic conditions and Γ is a scaling function for the production rate based on the difference in current stretch and homeostatic stretch of the collagen fibers

$$\delta = \lambda_{current}^{coll} - \lambda_{hom}. \quad (17)$$

The scaling function is taken from [15] as this allows saturation and a homeostatic production rate. It is defined as

$$\begin{cases} \Gamma = 0 & \delta < l_{neg} \\ \Gamma = \frac{1}{2}[1 + \sin(\omega_{neg}(\delta + b_{neg}))] & \delta \in [l_{neg}, 0) \\ \Gamma = \frac{1}{2}[(m_{max} + 1) + (m_{max} - 1)\sin(\omega_{pos}(\delta - b_{pos}))] & \delta \in [0, l_{pos}) \\ \Gamma = m_{max} & \delta > l_{pos}. \end{cases} \quad (18)$$

with $\omega_{neg} = 2K_{\sigma}$, $\omega_{pos} = \frac{2K_{\sigma}}{m_{max}-1}$, $l_{neg} = -\pi/\omega_{neg}$ and $l_{pos} = \pi/\omega_{pos}$. The degradation rate of collagen depends on the same mechanical stimulus δ through

$$q^{coll}(s, \tau) = \exp\left(-\sum_{\hat{\tau}=\tau}^s K_{qh}^{coll}(1 + \text{abs}(\delta))\Delta\tau\right). \quad (19)$$

The parameter K_{qh}^{coll} and the number of cohorts have an effect on the amount of physical time to which one growth step in Abaqus corresponds. Before the growth and remodeling algorithm starts, the collagen cohorts need to be initialized. We assume that the total amount of collagen initially has a fraction of 0.2 [14]. We also know that the collagen in the oldest cohort needs to be sufficiently degraded before being removed. Therefore, the collagen cohorts are initially filled according to

$$\rho_{\tau}^{coll} = m^0 * \exp(-(\tau - 1)K_{qh}^{coll})\Delta\tau. \quad (20)$$

The value of m^0 , the production under homeostatic conditions, needs to be determined using the assumption that under homeostatic conditions, *i.e.* when δ equals one, the

amount of collagen that is deposited matches the amount of collagen that is degraded. The total amount of collagen that is degraded is calculated by summing up the degradations per collagen cohort. Collagen cohort c degrades with an amount $\exp(-K_{q_h}^{coll}(c-1))$. Therefore, the total amount of collagen that degrades under homeostatic conditions is $\sum_{\tau}^{\tau_{max}-1} \exp(-K_{q_h}^{coll}(\tau-1))$. By dividing the initial collagen fraction with that factor, m^0 can be determined as

$$m^0 = \frac{\rho^{coll}(0)}{\sum_{\tau}^{\tau_{max}-1} \exp(-K_{q_h}^{coll}(\tau-1))\Delta\tau}. \quad (21)$$

We know that the half-life of collagen is around 70 days. If one time step of growth corresponds to one day, the value of the homeostatic decay constant of collagen is $K_{q_h}^{coll} = \log(2.0)/70days^{-1}$ [26, 27]. Therefore, changing the value of $K_{q_h}^{coll}$ changes the number of days to which one step in Abaqus corresponds. In this case, we assume that one step in Abaqus corresponds to 10 days. Therefore the value of $K_{q_h}^{coll}$ is set to $\log(2.0)/7$ and its units to $1/10days^{-1}$. Here, we chose to work with 60 cohorts of collagen and a time step of 10 days.

To determine the volumetric change due to growth, we divide the constituent density with the total current density. The difference between the total current density and the total initial density is used to drive volumetric growth. The volumetric growth is calculated using the same concept as kinematic growth, namely by multiplicatively decomposing the deformation gradient into a growth deformation gradient and an elastic gradient. Furthermore, we assume that growth only occurs in the radial direction, by deriving the volumetric growth gradient as

$$\mathbf{F}_{vol}(s) = \frac{\rho_{total}(s-1)}{\rho_{total}(0)} \mathbf{n} \otimes \mathbf{n}, \quad (22)$$

where \mathbf{n} corresponds to the radial direction. We used forward Euler to integrate the density evolution at each time step.

The constrained mixture approach uses several phenomenological assumptions. Most of these assumptions are taken from literature (see [14, 15]). However, two assumptions are novel to this work. First, the mechanical stimulus δ is chosen to be the difference in stretch, whereas previously it was chosen as a difference in tension. Second, the addition of the volumetric growth based on the difference in collagen fraction is novel to this work as well.

In equation 2, the SEDF depends on the global deformation and the Cauchy stress $\boldsymbol{\sigma}$ and the tangent stiffness tensor \mathbb{c}^{Abaqus} are calculated by deriving the SEDF with respect to the global deformation. In the CMT case, the SEDF is divided into a volumetric contribution and constituent contributions as can be seen in equation 13. The total Cauchy stress $\boldsymbol{\sigma}$ and tangent stiffness tensor \mathbb{c}^{Abaqus} are the sum of the volumetric and constituent specific contributions.

The constituent contributions depend on the constituent specific deformation and the derivation of the Cauchy stress and tangent stiffness tensor is slightly altered. The constituent specific deformation is calculated by multiplying the global deformation gradient with a constituent specific deformation tensor $\mathbf{F}^\alpha = \mathbf{F}\mathbf{G}_\alpha$. To derive the constituent specific Cauchy stress $\boldsymbol{\sigma}$, we go back to index notation,

$$\sigma_{ij}^\alpha = \frac{1}{J} \frac{\partial \Psi^\alpha}{\partial \bar{F}_{ia}} \bar{F}_{ja} \quad (23)$$

where α can be elastin or collagen.

The total Cauchy stress tensor equals

$$\boldsymbol{\sigma} = \sum_{\alpha=\text{elastin,collagen}} \boldsymbol{\sigma}^\alpha + \boldsymbol{\sigma}^{vol}. \quad (24)$$

To calculate the constituent specific tangent stiffness tensor, we start from equation 5, which becomes

$$\mathbb{C}_{ijkl}^{\alpha, \text{Abaqus}} = \sigma_{ij}^\alpha \delta_{kl} + \frac{1}{2} \left(\frac{\partial \sigma_{ij}^\alpha}{\partial \bar{F}_{ka}} \bar{F}_{la} + \frac{\partial \sigma_{ij}^\alpha}{\partial \bar{F}_{la}} \bar{F}_{ka} \right). \quad (25)$$

The total tangent tensor equals

$$\mathbb{C}_{ijkl}^{\text{Abaqus}} = \sum_{\alpha=\text{elastin,collagen}} \mathbb{C}_{ijkl}^{\alpha, \text{Abaqus}} + \sigma_{ij}^{vol} \delta_{kl} + \frac{1}{2} \left(\frac{\partial \sigma_{ij}^{vol}}{\partial F_{ka}} F_{la} + \frac{\partial \sigma_{ij}^{vol}}{\partial F_{la}} F_{ka} \right). \quad (26)$$

2.5 Comparison to experimental data

We created a virtual counterpart of the unreinforced experiment of [18], both for the kinematic growth and for the constrained mixture approach, in the finite element software *Abaqus 2017* (Dassault Systèmes, Providence, RI, USA). A finite element model requires a geometry, a material description, as well as boundary and loading conditions.

Both approaches start from the geometry of the interposition graft in aortic position that was segmented from MRI images taken at day four using *3-Matic 13.0* (Materialise, Leuven, Belgium). The obtained geometry was spatially discretized in a hexahedral mesh using the geometrical and finite element analysis pre- and postprocessing software *pyFormex* [28] (University of Ghent, Belgium).

The constitutive material parameters for the different tissue types (native aorta and native pulmonary artery) present in the finite element model are inferred from biaxial tissue testing experiments [18], as discussed by Maes *et al.* [29]. These parameters can be found in Table 2. For one sheep, no converged parameters could be found and this sheep was excluded. During surgery, the aortic pressure was measured as well as the imposed axial prestretch on the autograft (Table 1).

Figure 3 describes our computational workflow to virtually replicate the biomechanical loading and remodeling of the studied pulmonary autografts during our clinical study. This workflow can be subdivided in three simulations.

The first simulation represents the pulmonary artery that is placed in aortic position. This simulation serves several purposes. First, this simple geometry serves as an initial validation of the model. Next, it also allows to determine the prestressed situation of the sheep-specific geometry at aortic position and it will be used to compare the results of the real geometry with the idealized cylinder. First, a cylindrical pulmonary artery is inflated at pulmonary pressure (0.00208 MPa [30]) and the deposition stretches are determined [23, 24]. (Briefly, the geometry is inflated, the resulting deformation gradient is imposed as a deposition stretch tensor on the deformed geometry. In the following steps, the remaining deformation is again imposed as a deposition stretch tensor until the prestretched geometry is obtained.) Next, this pulmonary artery with deposition stretches is inflated to aortic pressure and the experimentally measured axial prestretch is imposed. The stretch the collagen fibers feel at that point is stored as λ_{hom} and we have determined the prestressed situation of the geometry at aortic position. Finally, this geometry will also grow for six months so that we can compare the results of the ideal cylinder with the results of the real geometry.

In the second simulation, the stretches the collagen fibers feel in aortic position are assigned to the pulmonary autograft in the segmented geometry of the MRI taken at day four. The axial prestretches are assigned to the different tissues as well. The prestressed situation of the real geometry is then determined similarly to the deposition stretches. After finding the prestressed situation, the geometry is allowed to grow for six months using either kinematic growth or constrained mixture growth. At the end of the six months, the fractions of elastin and collagen, the remaining elastin deformation and collagen stretch are stored for the constrained mixture approach and transferred to a simulation of a virtual biaxial test. For kinematic growth, the volumetric change θ is stored. More details on the finite element model can be found below.

The third set of simulations are virtual biaxial experiments. Given that the kinematic growth theory does not induce any changes to the underlying constituents of the material, the material stiffness of the tissue will not change in that framework. Therefore, we only perform virtual biaxial experiments for our CMT simulations. From the virtually grown geometries, two samples for virtual biaxial experiments are extracted: one located at the bulging side of the autograft and one on the nonbulging side. The biaxial sample is created by virtually extracting a piece of the deformed geometry to which the different fractions and deformations of the collagen fibers and elastin are assigned. Next, this sample is loaded biaxially, by imposing a displacement on the longitudinal and circumferential sides while constraining one edge in the vertical direction. This virtual experiment is performed on the sample before growth (to resemble baseline behavior), after 10 days of growth, 50 days and 180 days of growth.

Details on the finite element models Three different finite element models are constructed per sheep: ideal cylinder, sheep-specific geometry and two biaxial samples.

The ideal cylinder is modeled as half a cylinder with symmetry boundary conditions as shown in Figure 4. The diameter is 18mm (this is an estimated average for a pulmonary artery of this strain and age of sheep), the unloaded thickness is sheep-specific and is taken as the *in vivo* thickness determined in the parameter fitting (see Table 2). The pressure, either pulmonary pressure (0.00208 MPa from [30]) or aortic pressure (as measured during surgery, see Table 1) is imposed on the inner surface of the cylinder. The geometry is meshed using hexahedral elements with four elements through the thickness.

In the sheep-specific thoracic aorta, three different sections are defined: the pulmonary autograft, the aorta located proximally and the aorta located distally with respect to this autograft. For each of these sections, different constitutive material properties were assigned. The proximal and distal ends of the thoracic aorta are fixed in the longitudinal and radial direction and the aortic pressure is imposed on the inner surface. The geometry is meshed using reduced hexahedral elements and for each sheep a mesh convergence study is conducted. In this mesh convergence study, the average collagen fraction after 180 days of growth is used as convergence criterion. We assumed our geometrical discretization to be adequate when this value changes less than 1 %. Since the elements are reduced, an hourglass stiffness needs to be defined. Following [31], the hourglass stiffness was set to 1.5 MPa (except for the simulations of sheep 3 and 5, where the hourglass stiffness is 3 MPa). To check that this hourglass correction does not result in unphysical results, the artificial strain energy is checked to be sufficiently low for each simulation.

The geometry of the virtual biaxial test is created by taking a patch of elements from the sheep-specific geometry with their deformation at the time of interest. The simulation consists of three steps: importing solution dependent variables, releasing the kinematic boundary conditions on the geometry and performing the virtual biaxial test. Figure 5 schematically visualizes the different boundary conditions. In the first step, all nodes of the geometry are fixed while the solution dependent variables, which include the collagen fractions, the deformation history of collagen, and the deposition stretch tensor, are imported. The second step releases the virtual biaxial sample, by fixing the top surface in the vertical direction and the two sets of sides that will be displaced in the next step are fixed in the direction in which they will be displaced.

In all simulations, hybrid elements are used with the total hybrid formulation. Finally, all simulations are performed in Abaqus standard. In the growth step, ‘*Controls, analysis=discontinuous’ is added since it improves efficiency for severely discontinuous behavior. Adding this parameter results in an increased number of iterations before the convergence rate is checked. [32].

3 Results

This section presents the results of the different simulations. The results of sheep 1 and sheep 2 are given. The pulmonary autograft of the former sheep has a shape that resembles a perfect cylinder more closely, whereas sheep 2 has a pulmonary autograft geometry that is very noncylindrical. The results of the other sheep are given in the appendix.

Figures 6 and 7 show the growth factor value for the KG in the circumferential direction at 10 days, 50 days and 180 days of growth. The growth factor slowly increases over time and the corresponding change in diameter is visible in the autograft.

Figures 8 and 9 show the collagen fraction present at 10 days, 50 days and 180 days for two sheep for the CMT. Both figures show a similar trend. Removal of collagen is already apparent after 10 days, and more pronounced after 50 days. At 180 days, the collagen fraction appears to have stabilized compared to the situation at 50 days, but the diameter of the autograft section increases. Additionally, removal of collagen in the normal aorta at the edge of the autograft becomes visible at 180 days. The results of the other sheep can be found in the appendix.

Figure 10 visualizes the average collagen fraction over the autograft over time. All sheep show the same trend in average collagen fraction: a decrease until it reaches a minimum after which it starts to increase. As we only have experimental data until 180 days, the simulations with the segmented geometry only go to 180 days. The collagen fraction of the ideal cylinder appears to converge after a while, though not to the initially imposed homeostatic value of 0.2.

Figures 11 and 12 show the stress-stretch curves of the virtual biaxial experiments of a sample on the bulging side and on the nonbulging side of the autograft respectively for sheep 1 and sheep 2. Note that these virtual experiments are only performed for the CMT simulations as the kinematic growth simulations do not induce changes to the material stiffness. Each sample is tested before growth (baseline), after 10 days, 50 days and 180 days. The left two figures correspond to the stress-stretch curves of the sample on the bulging side in the circumferential and axial direction. The right two figures correspond to the results of the sample on the nonbulging side. The results of the other sheep can be found in appendix.

Figure 13 shows how the diameter changes over time using the CMT and the kinematic-based growth approach. It also shows the experimentally measured values previously reported by [18]. The experimental values all show an initial steep increase, followed by a less drastic increase. The simulations on the other hand show a linear increase of the diameter over time.

4 Discussion

4.1 Kinematic Growth

Kinematic-based growth starts by decomposing the deformation gradient into a growth deformation gradient and an elastic deformation gradient. The growth deformation gradient needs to be constitutively prescribed in the model. Therefore, kinematic-based growth does not introduce a change in mechanical behavior of the tissue but allows the geometry to deform based on the prescribed growth deformation gradient.

Figures 6 and 7 show a similar trend in the change of the growth factor over time, *i.e.* a slow increase, despite having a different axial prestretch (1.3 *vs.* 1.6) and having severely different geometries. Sheep 1 has a geometry that is closer to a cylinder, whereas sheep 2 has an initial geometry where the autograft bulges out much more. Looking more closely at both figures, we can see that the value of the growth factor changes through the thickness of the geometry. This can be expected as the stretch the collagen fibers feel is different throughout the thickness. Additionally, the value of the growth factor over the autograft is more uniform in Figure 6 compared to Figure 7, where the growth factor clearly differs within the autograft. This is a result of the difference in geometry, causing a less uniform distribution in the collagen stretch in the latter case.

4.2 Constrained Mixture Theory

Figures 8 and 9 show how the collagen fraction is distributed 10 days, 50 days and 180 days after surgery, when using the CMT. Comparing the situation at 10 days with the situation at 50 and 180 days, shows that the collagen fraction first drops and then recovers. The distribution of the collagen fraction at 50 days and 180 days appears to be more uniform in sheep 1 compared to sheep 2. This was also the case for the growth factor distribution in the kinematic growth simulations. This makes sense since both types of simulations (CMT and KG) use the stretch the collagen fibers feel as the biomechanical stimulus for growth and remodeling. To demonstrate this, Figure 14 shows the average stretch in the collagen fibers at the start of growth. Within the autograft, this value deviates severely from the homeostatic value of 1.1, resulting in remodeling.

The geometry changes significantly over time in these simulations. This geometry change is a result of the collagen fibers being removed and replaced by collagen fibers that are less prestretched. Placing the autograft in aortic conditions causes the collagen fibers to be severely stretched. When remodeling starts, these fibers are gradually removed and replaced by new fibers. These new fibers are deposited using their homeostatic stretch level. This stretch is lower than that of the removed collagen fibers, causing a change in intrinsic material stiffness, leading the vessel wall to bulge out under a continuous loading. Over time, this continuous dilatation of the autograft starts to affect the aortic sections as well, where fiber overstretching again results in collagen fraction changes.

This change is still limited to the area close to the border with the pulmonary autograft. Also, the area of the aorta that has a changing collagen fraction is much larger in sheep 2.

Within this computational study, a non-homogenized version of the CMT is employed, as it is conceptually simple allowing a more straightforward comparison and interpretation of the simulated outcomes. One of the main disadvantages of this version, is the high computational cost associated to the need of tracking all the previous configurations of collagen. The homogenized version of the CMT provides a lower computational costs while maintaining a mechanobiological motivation [8, 33, 34].

4.3 Comparison with experimental data

Figure 13 indicates how well the simulations are able to resemble the diameter change that was measured experimentally. All sheep show a diameter increase, but where the experimental values initially show a steep increase followed by a lower increase, the models show a more linear increase. Note that care should be taken when looking at the experimental data, as these measurements depend on the blood pressure of the sheep, which can naturally fluctuate. For the kinematic growth model, we chose to work with a law similar to Saez *et al.* who simulated hypertensive growth in the carotid [11]. Changing this law (*e.g.* making it a stress-driven as in the second implementation by Saez *et al.* [11] or adapting the function $k(\theta)$ [35]) and optimizing parameters will likely improve the model. However, before being able to improve the implemented laws, more experimental data is needed, preferably with a higher time resolution.

The CMT also shows a linear increase in diameter. This increase is a consequence of removing highly stretched collagen and replacing it with lesser stretched collagen. We expect this increase to stop when the collagen fraction stabilizes and a new stable situation is found. At 180 days our models are not yet in a stable situation. The stability of the experimental situation at 6 months, was also not evaluated as this would have required longer animal experiments. However, when assuming a turnover rate of collagen of 70 days, which is also found experimentally [27], it is not unexpected that the situation is not stable after 6 months. The effect of the turnover rate of collagen and its value need to be experimentally investigated further. Again, this mismatch is a consequence of the choice of equations and parameters and more focused studies are needed to determine these.

To compare our simulation results with the animal experiments, virtual biaxial tests were performed on two samples for each sheep: one sample on the bulging side of the autograft and one sample on the nonbulging side. Figures 11 to 12 show the stress-stretch curves for two sheep. Within these figures, a clear trend is visible, namely that the tissue stiffening occurs at higher stretch values after remodeling took place. This can again be linked with the highly stretched collagen fibers that are replaced with collagen fibers with a lower stretch. The virtual stress-stretch curves reach high stress values. This comes from the fact that there is no failure implemented in our constitutive behav-

ior. Moreover, there is pulled on the full sides of the sample, whereas in the mechanical experiments there is pulled with rakes.

The change in mechanical behavior is more pronounced in our virtual biaxial tests as in the experimental case, which can be seen in Figures 11 to 12. In general, the experimental stress-stretch curves are much lower and their nonlinear stiffening effect occurs later. Several possible reasons exist. First, within the experiments, the samples were mounted using rakes, which puncture five holes in each side of the sample. This causes local damage on the tissue and even the deformation of the sample is influenced by this mounting mechanism [36]. Second, in our virtual experiments, our samples are not completely released before performing the test, causing the stresses that are initially present in our virtual sample to be higher. Third, in our virtual test, we test the exact same sample at different timepoints, which is experimentally not feasible. A final reason is that our model does not yet capture all the occurring remodelling phenomena.

For both sheep, the stress-stretch curves of both samples within one sheep are different. If we focus on the baseline behavior stress-stretch curves, the difference is rather small in case of sheep 1 but in sheep 2 the difference between the baseline behavior of the sample on the bulging and on the nonbulging side is more pronounced. The difference in baseline behavior, despite having the same material parameters and constituent fractions at that time point, comes from the fact that the prestressed situation causes the elastin to have a regionally varying prestretch to counteract the aortic pressure.

In sheep 1, where the geometry resembles the cylindrical case more closely, the difference in stress-stretch curves over time between both samples is small and it appears that both samples show similar remodeling behavior. Contrarily, in sheep 2 the sample on the bulging side of the autograft remodels differently compared to the sample on the non bulging side. Previous figures already demonstrated that due to the removal of highly stretched collagen, the diameter increases. Due to the asymmetry of the autograft geometry, this increase in diameter causes the remaining and newly deposited collagen fibers on the bulging side of the autograft to be stretched more than the collagen on the nonbulging side. The sample on the bulging side of the autograft appears to lose its nonlinearity much more quickly compared to the other sample. As the collagen fibers on the bulging side are more stretched, they are more quickly degraded and the highly stretched collagen fibers are removed more quickly than on the nonbulging side. The experimental curves show a similar trend: the pulmonary autograft samples of sheep 1 almost coincide, whereas a slightly larger spread is visible in the stress-stretch curves of the pulmonary autograft samples of sheep 2.

Averaging the collagen fraction over the autograft leads to Figure 10. For comparison purposes the average fraction of an ideal cylinder is added to this figure as well. All sheep show a similar trend: all fractions initially decrease followed by a more slow increase. Within the animal experiment, the collagen content was measured in the native

pulmonary artery and in the pulmonary autograft at around 180 days, which revealed a doubling of the amount of collagen fibers. These collagen fibers most likely result from an inflammation-driven deposition of collagen in the *adventitia*. Within our model, no inflammation is taken into account and only the deviation of the collagen stretch of its homeostatic value drives the growth and remodeling processes [37].

4.4 Comparison between kinematic growth and constrained mixture based models

The kinematic-based growth can capture the trend of the geometrical change occurring throughout the experiment. The CMT also captures this increase of diameter and is able to qualitatively model the change in mechanical behavior. An important difference between both types of models is that the kinematic growth approach predicts an increase in mass (as the growth factor becomes greater than 1), whereas the constrained mixture approach shows a decreasing collagen fraction, leading to a decrease in mass. The experimental observations of [18] show an increase in collagen, mainly due to inflammation deposition, in the *adventitia*. However, the medial thickness decreases prominently. Since inflammation deposition is currently not modelled, a decrease in collagen is expected within the simulations, making the current implementation of the kinematic based approach not suitable for simulating what is occurring experimentally. Looking further into the triggers of growth and adapting the law of the growth factor can possibly overcome this limitation. When modelling the inflammation deposition of collagen, it is important that the relation between collagen production and removal is computationally investigated.

To decide on the type of model to use for a growth and remodelling simulation the following considerations can be made. In case the change in geometry is the most relevant aspect, kinematic growth models can be advised, noting that the stimulus of growth and the corresponding growth deformation need to be known or postulated. When the change in constituent fractions and corresponding change in mechanical behavior need to be simulated as well, CMT is needed. In this case, again the stimulus of growth needs to be defined as well as expressions for turnover and degradation rates need to be known or postulated.

4.5 Future work

The CMT assumes that an artery is composed out of several constituents. The current implementation is limited to elastin and collagen. The histological analysis of [18] show a high amount of smooth muscle cells present in the arterial wall. Including the smooth muscle cells would render this implementation more biofidelic, but results in an increased computational cost and as the increased blood pressure most likely incapacitates the active behavior of smooth muscle cells on the pulmonary autograft, the error resulting from this assumption is expected to be limited. Nevertheless, future studies should definitely

investigate what happens with the smooth muscle cells in the pulmonary autograft, both experimentally and computationally. Moreover, the artery is modelled here as a uniform layer, whereas in reality, an artery consists of multiple layers (intima, media, adventitia). The experimental results show that the collagen deposition in the pulmonary autograft is focused in the adventitial layer [18]. However, the mechanical data represents the artery as a uniform material, as the mechanical tests do not allow to test the arterial layers separately. Further improving the biofidelity of this model should also consider the layer-specificity. When increasing the biofidelity of the model, care should be taken when increasing the amount of parameters. The current implementation already has a high amount of parameters and evaluating the effect of each parameter on the outcome is unfeasible. Therefore, when postulating new laws, the amount of parameters should be closely monitored. Performing a computational study similar to Ramachandra *et al.*, who numerically investigated the bounds of the different parameters for vein graft remodeling [38], can also bring added value.

Ultimately, these type of growth and remodeling models can be used to perform surgical design optimization studies, reducing the need for technically and ethically challenging animal and clinical trials. It would for example be interesting to evaluate how variables that are surgically imposed, such as the axial prestretch on the autograft, influence the outcome of the procedure in terms of final geometry and wall stress. Nevertheless, before such models can be used in so called *in silico* trials, more certainty is required regarding the input parameters that were used and the laws that were imposed. However, the relevance of *in silico* trials can not be understated as nicely described in this review paper focusing on cardiac modeling [39].

Several parameters in the used models, both KG and CMT, were arbitrarily chosen or taken from literature. How their value affects the outcome of these models should be investigated in a parameter sensitivity study. As for the various imposed laws, *e.g.* equation 7 in the KG approach or equations 16 and 19 in the CMT, are taken from literature and require experimental verification. More controlled experiments, such as bioreactor experiments, where one specific parameter can be changed, should be conducted to evaluate these laws. These types of experiments might also aid in determining whether it is stress or stretch that drives growth. In previous work [14], stress was the stimulus for growth. However, here, we chose to work with stretch. Within literature, there is still no consensus what triggers growth. The implemented models in combination with more controlled experiments might help to improve our understanding of the growth and remodeling phenomena, and ultimately result in reliable *in silico* trials.

5 Conclusion

Several theories exist that try to capture the growth and remodeling processes in soft tissues. The two most used approaches are kinematic-based growth theory and constrained mixture theory. Where the former focuses more on geometrical changes that

occur, the latter starts from a more mechanobiological perspective. When applying both types of theories on the same experimental data, their differences became clear. The kinematic-based growth is capable of simulating the circumferential growth that occurred in a pulmonary autograft. The CMT was capable of showing the dilatation of the pulmonary autograft as well. A change in collagen fraction and corresponding change in mechanical behavior was captured by the CMT. Whichever theory should be used for a certain experiment, depends on where the interest lies: geometrical changes can be captured by KG; changing constituents and mechanical behavior can be described with CMT.

Acknowledgements

This work was supported by a C2 project (ADAPT) of the KU Leuven and three doctoral grants (SB 1S56317N, SB 1S35316N, 11A6519N) and a postdoctoral fellowship (PD0/012) of the Research Foundation Flanders (FWO). It was also supported by travel grants granted by Research Foundation Flanders and the Snoeys foundation.

References

- [1] M. Viceconti, F. Pappalardo, B. Rodriguez, M. Horner, J. Bischoff, F. Musuamba Tshinanu, In silico trials: Verification, validation and uncertainty quantification of predictive models used in the regulatory evaluation of biomedical products, *Methods* (2020). doi:10.1016/j.ymeth.2020.01.011.
- [2] E. K. Rodriguez, A. Hoger, A. D. McCulloch, Stress-dependent finite growth in soft elastic tissues, *Journal of Biomechanics* 27 (4) (1994) 455–467. doi:10.1016/0021-9290(94)90021-3.
URL <https://www.sciencedirect.com/science/article/pii/0021929094900213?via=ihub>
- [3] J. D. Humphrey, K. R. Rajagopal, A constrained mixture model for growth and remodeling of soft tissues, *Mathematical Models and Methods in Applied Sciences* 12 (03) (2002) 407–430. doi:10.1142/S0218202502001714.
URL <https://www.worldscientific.com/doi/abs/10.1142/S0218202502001714>
- [4] P. Watton, N. Hill, M. Heil, A mathematical model for the growth of the abdominal aortic aneurysm, *Biomechanics and Modeling in Mechanobiology* (3) (2004) 98–113. doi:10.1007/s10237-004-0052-9.
- [5] S. Baek, K. Rajagopal, H. J.D., A theoretical model of enlarging intracranial fusiform aneurysms, *Journal of Biomechanical Engineering* 1 (128) (2006) 142–149. doi:10.1115/1.2132374.

- [6] J. D. Humphrey, G. A. Holzapfel, Mechanics, mechanobiology, and modeling of human abdominal aorta and aneurysms, *Journal of Biomechanics* 45 (3) (2012) 805–814. doi:10.1016/j.biomech.2011.11.021.
URL <https://www.worldscientific.com/doi/abs/10.1142/S0218202502001714>
- [7] T. C. Gasser, A. Grytsan, Biomechanical modeling the adaptation of soft biological tissue, *Current Opinion in Biomedical Engineering* 1 (2017) 71–77.
- [8] C. J. Cyron, R. C. Aydin, J. D. Humphrey, A homogenized constrained mixture (and mechanical analog) model for growth and remodeling of soft tissue, *Biomechanics and Modeling in Mechanobiology* 15 (6) (2016) 1389–1403. doi:10.1007/s10237-016-0770-9.
- [9] M. Latorre, Modeling biological growth and remodeling: Contrasting methods, contrasting needs, *Current Opinion in Biomedical Engineering* 15 (2020) 26–31. doi:10.1016/j.cobme.2019.11.005.
URL <https://doi.org/10.1016/j.cobme.2019.11.005>
- [10] A. Schäfer, J. Weickenmeier, E. Kuhl, The interplay of biochemical and biomechanical degeneration in Alzheimer’s disease, *Computer Methods in Applied Mechanics and Engineering* 352 (2019) 369–388. doi:10.1016/j.cma.2019.04.028.
URL <https://doi.org/10.1016/j.cma.2019.04.028>
- [11] P. Sáez, E. Peña, M. A. Martínez, E. Kuhl, Computational modeling of hypertensive growth in the human carotid artery, *Comput Mech* 53 (2014) 1183–1196. doi:10.1007/s00466-013-0959-z.
URL <http://biomechanics.stanford.edu/paper/CMECH14.pdf>
- [12] A. M. Zöllner, M. A. Holland, K. S. Honda, A. K. Gosain, E. Kuhl, Growth on demand: Reviewing the mechanobiology of stretched skin, *Journal of the Mechanical Behavior of Biomedical Materials* 28 (2013) 495–509. doi:10.1016/j.jmbbm.2013.03.018.
- [13] M. Peirlinck, F. Sahli Costabal, K. L. Sack, J. S. Choy, G. S. Kassab, J. M. Guccione, M. De Beule, P. Segers, E. Kuhl, Using machine learning to characterize heart failure across the scales, *Biomechanics and Modeling in Mechanobiology* 18 (6) (2019) 1987–2001. doi:10.1007/s10237-019-01190-w.
URL <https://doi.org/10.1007/s10237-019-01190-w>
- [14] N. Famaey, J. Vastmans, H. Fehervary, L. Maes, E. Vanderveken, F. Rega, S. J. Mousavi, S. Avril, Numerical simulation of arterial remodeling in pulmonary autografts, *ZAMM - Journal of Applied Mathematics and Mechanics / Zeitschrift für Angewandte Mathematik und Mechanik* 98 (12) (2018) 2239–2257. doi:10.1002/zamm.201700351.
URL <https://onlinelibrary.wiley.com/doi/full/10.1002/zamm.201700351>

- [15] A. Valentin, J. D. Humphrey, G. A. Holzapfel, A finite element-based constrained mixture implementation for arterial growth, remodeling, and adaptation: Theory and numerical verification, *International Journal for Numerical Methods in Biomedical Engineering* 29 (1) (2013) 822–849. doi:10.1002/cnm.2555.
URL <https://onlinelibrary.wiley.com/doi/full/10.1002/cnm.2555>
- [16] C. J. Cyron, J. D. Humphrey, Growth and remodeling of load-bearing biological soft tissues, *Meccanica* (2017). doi:10.1007/s11012-016-0472-5.
- [17] D. Ambrosi, M. B. Amar, C. J. Cyron, A. DeSimone, A. Goriely, J. D. Humphrey, E. Kuhl, Growth and remodelling of living tissues: Perspectives, challenges and opportunities, *Journal of the Royal Society Interface* 16 (157) (2019). doi:10.1098/rsif.2019.0233.
- [18] E. Vanderveken, J. Vastmans, P. Claus, E. Verbeken, H. Fehervary, L. Van Hoof, K. Vandendriessche, P. Verbrugghe, N. Famaey, F. Rega, Mechano-biological adaptation of the pulmonary artery exposed to systemic conditions, *Scientific Reports* 10 (1) (2020) 1–12. doi:10.1038/s41598-020-59554-7.
- [19] T. C. Gasser, R. W. Ogden, G. A. Holzapfel, Hyperelastic modelling of arterial layers with distributed collagen fibre orientations., *Journal of the Royal Society, Interface / the Royal Society* 3 (6) (2006) 15–35. arXiv:0312002v1, doi:10.1098/rsif.2005.0073.
- [20] H. Fehervary, L. Maes, J. Vastmans, G. Kloosterman, N. Famaey, On the use of user-defined materials for fiber-reinforced hyperelastic materials, *Journal of the Mechanical Behavior of Biomedical Materials* (2020) 103737doi:10.1016/j.jmbbm.2020.103737.
URL <https://linkinghub.elsevier.com/retrieve/pii/S1751616120302915>
- [21] M. A. Holland, The Hitchhiker’s Guide to Abaqus, <https://zenodo.org/record/1243270#.X2CHRygzY2w>, accessed: 2020-09-15 (2017). doi:10.5281/zenodo.1243269.
- [22] L. Maes, J. Vastmans, S. Avril, N. Famaey, A chemomechanobiological model of the long-term healing response of arterial tissue to a clamping injury, *Frontiers in Bioengineering and Biotechnology*.
- [23] S. J. Mousavi, S. Avril, Patient-specific stress analyses in the ascending thoracic aorta using a finite-element implementation of the constrained mixture theory, *Biomechanics and Modeling in Mechanobiology* 16 (5) (2017) 1765–1777. doi:10.1007/s10237-017-0918-2.
URL <http://link.springer.com/10.1007/s10237-017-0918-2>
- [24] C. Bellini, J. Ferruzzi, S. Roccabianca, E. S. Di Martino, J. D. Humphrey, A microstructurally motivated model of arterial wall mechanics with mechanobiological implications, *Annals of Biomedical Engineering* 42 (3) (2014) 488–502. arXiv:NIHMS150003, doi:10.1007/s10439-013-0928-x.

- [25] M. J. Sherratt, Tissue elasticity and the ageing elastic fibre, *Age* 31 (4) (2009) 305–325. doi:10.1007/s11357-009-9103-6.
- [26] A. Valentín, J. D. Humphrey, Parameter sensitivity study of a constrained mixture model of arterial growth and remodeling, *Journal of Biomechanical Engineering* 131 (10) (2009) 1–11. doi:10.1115/1.3192144.
- [27] R. Nissen, G. J. Cardinale, S. Udenfriend, Increased turnover of arterial collagen in hypertensive rats, *Proceedings of the National Academy of Sciences of the United States of America* 75 (1) (1978) 451–453. doi:10.1073/pnas.75.1.451.
- [28] B. Verheghe, pyFormex, <http://www.nongnu.org/pyformex/>.
- [29] L. Maes, H. Fehervary, J. Vastmans, S. J. Mousavi, S. Avril, N. Famaey, Constrained mixture modeling affects material parameter identification from planar biaxial tests, *Journal of the Mechanical Behavior of Biomedical Materials* 95 (April) (2019) 124–135. doi:10.1016/j.jmbbm.2019.03.029.
URL <https://doi.org/10.1016/j.jmbbm.2019.03.029>
- [30] D. Bia, R. Armentano, D. Craiem, J. Grignola, F. Ginés, A. Simon, J. Levenson, Smooth muscle role on pulmonary arterial function during acute pulmonary hypertension in sheep, *Acta Physiologica Scandinavica* 181 (3) (2004) 359–366. doi:10.1111/j.1365-201X.2004.01294.x.
- [31] S. D. Systemes, Hourglass stiffness, Abaqus Keywords Reference Guide, 6th Edition. URL <http://abaqus.software.polimi.it/v6.14/books/key/default.htm>
- [32] S. D. Systemes, Abaqus Documentation Collection, 6th Edition. URL <http://abaqus.software.polimi.it/v6.14/index.html>
- [33] F. Braeu, A. Seitz, R. Aydin, C. Cyron, Homogenized constrained mixture models for anisotropic volumetric growth and remodeling, *Biomechanics and Modeling in Mechanobiology* (2017) 889–906 doi:10.1007/s10237-016-0859-1.
- [34] S. J. Mousavi, S. Farzaneh, S. Avril, Patient-specific predictions of aneurysm growth and remodeling in the ascending thoracic aorta using the homogenized constrained mixture model, *Biomechanics and Modeling in Mechanobiology* 18 (6) (2017) 1895–1913. doi:10.1007/s10237-019-01184-8.
- [35] E. Kuhl, R. Maas, G. Himpel, A. Menzel, Computational modeling of arterial wall growth, *Biomechanics and Modeling in Mechanobiology* 6 (5) (2007) 321–331. doi:10.1007/s10237-006-0062-x.
URL <http://link.springer.com/10.1007/s10237-006-0062-x>
- [36] H. Fehervary, M. Smoljkić, J. Vander Sloten, N. Famaey, Planar biaxial testing of soft biological tissue using rakes: A critical analysis of protocol and fitting process, *Journal of the Mechanical Behavior of Biomedical Materials* (2016). doi:10.1016/j.jmbbm.2016.01.011.

- [37] M. Latorre, B. Spronck, J. D. Humphrey, Complementary roles of mechanotransduction and inflammation in vascular homeostasis, *Proceedings of the Royal Society A: Mathematical, Physical and Engineering Sciences* 477 (2245) (2021) 20200622. doi:10.1098/rspa.2020.0622.
URL <https://royalsocietypublishing.org/doi/10.1098/rspa.2020.0622>
- [38] A. B. Ramachandra, S. Sankaran, J. D. Humphrey, A. L. Marsden, Computational Simulation of the Adaptive Capacity of Vein Grafts in Response to Increased Pressure, *Journal of Biomechanical Engineering* 137 (3) (2015) 1–10. doi:10.1115/1.4029021.
- [39] M. Peirlinck, F. S. Costabal, J. Yao, J. M. Guccione, S. Tripathy, Y. Wang, D. Ozturk, P. Segars, T. M. Morrison, S. Levine, E. Kuhl, Precision medicine in human heart modeling, *Biomechanics and Modeling in Mechanobiology* (feb 2021). doi:10.1007/s10237-021-01421-z.
URL <http://link.springer.com/10.1007/s10237-021-01421-z>

Tables

Table 1: Experimentally measured variables. * no pressure measurement was obtained during surgery, therefore average pressure of other sheep is used.

Sheep	Diastolic aortic pressure [MPa]	Diastolic aortic pressure [mmHg]	Axial prestretch [-]
1	0.00613	45.98	1.3
2	0.00573*	42.98	1.6
3	0.00427	32.03	1.2
4	0.00573*	42.98	1.3
5	0.00707	53.03	1.2
6	0.00547	41.03	1.4

Table 2: GOH material parameters for the pulmonary artery samples.

^o The thickness values between brackets correspond to the thickness the pulmonary artery has when placed in aortic position

^x No converged parameters were found for this sample, the parameters of the distal aorta are used

⁺ No converged parameters were found for this sample, the parameters of the proximal aorta are used

	Sheep	C ₁₀ [MPa]	k ₁ [MPa]	k ₂ [-]	κ [-]	α [rad]	<i>in vivo</i> thick. [mm]
Pulmonary artery ^o	1	0.0029	0.0026	1.8988	0.1606	0.5854	2.80(1.89)
	2	0.0027	0.0044	0.7353	0.1213	0.4486	2.05(1.42)
	3	0.0027	0.0058	12.9093	0.2154	0.0056	1.45(1.16)
	4	0.0026	0.0062	7.776	0.2438	0.0126	1.80(1.37)
	5	0.0046	0.003	8.7905	0.2167	0.406	1.53(1.13)
Proximal aorta	1	0.0073	0.0391	0.0261	0.2084	0.4009	1.93
	2	0.0111	0.0104	0.0007	0.1727	0.0011	2.41
	3	0.0098	0.0037	0.0001	0	0.0002	2.19
	4 ^x	0.0066	0.0114	1.6236	0	0.6161	1.66
	5	0.0059	0.0233	0.5248	0.1777	0.5618	2.44
Distal aorta	1 ⁺	0.0073	0.0391	0.0261	0.2084	0.4009	1.93
	2	0.0129	0.0043	0.0001	0	0.0003	3.18
	3	0.0092	0.003	0.0001	0	0.0003	2.29
	4	0.0066	0.0114	1.6236	0	0.6161	1.66
	5	0.0066	0.0213	0.014	0.0879	0.5073	1.73

Figures

Figure 1

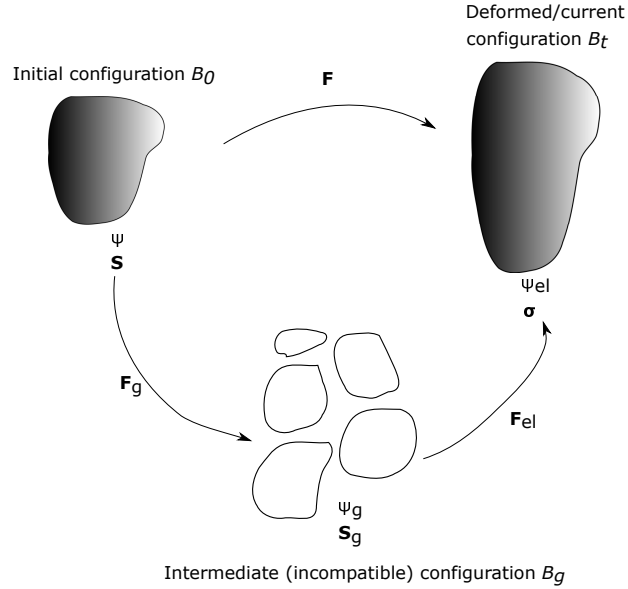


Figure 1: **The different configurations present in the kinematic-based growth theory.** The total deformation gradient \mathbf{F} can be multiplicatively decomposed into an elastic deformation gradient \mathbf{F}_{el} and a growth deformation gradient \mathbf{F}_g . The Cauchy stress $\boldsymbol{\sigma}$ can be expressed in the deformed configuration, whereas the second Piola-Kirchhoff stress can be expressed in the initial configuration \mathbf{S} or in the intermediate configuration \mathbf{S}_g . The strain energy density function Ψ can be derived in each configuration.

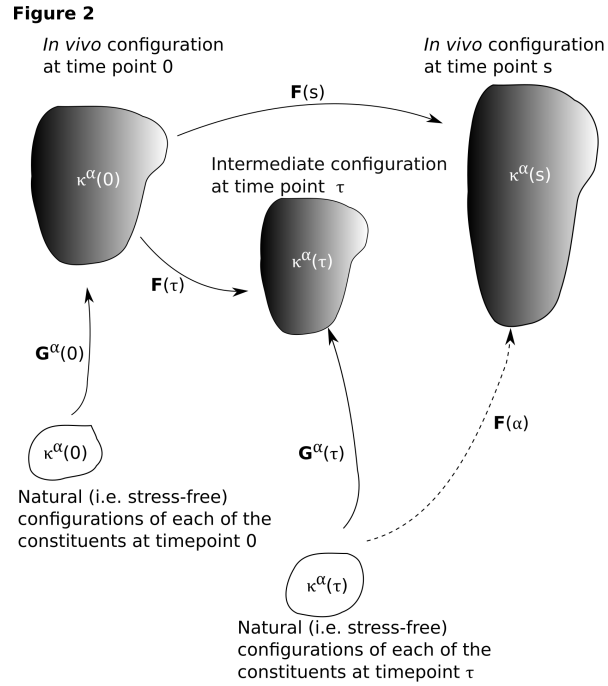
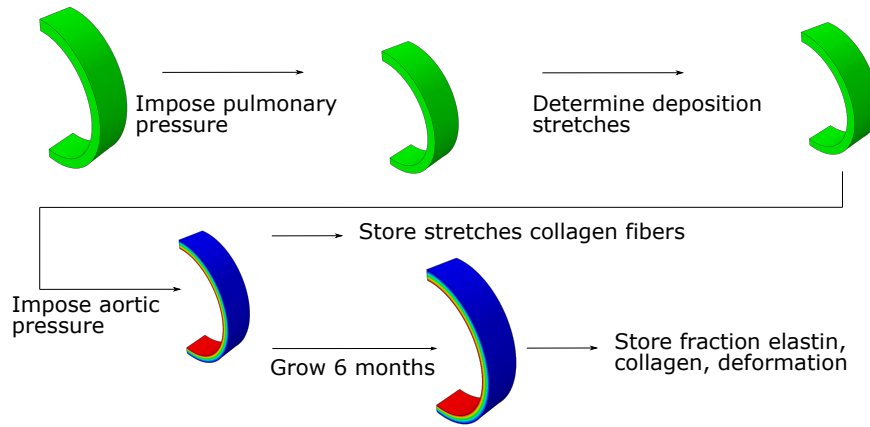
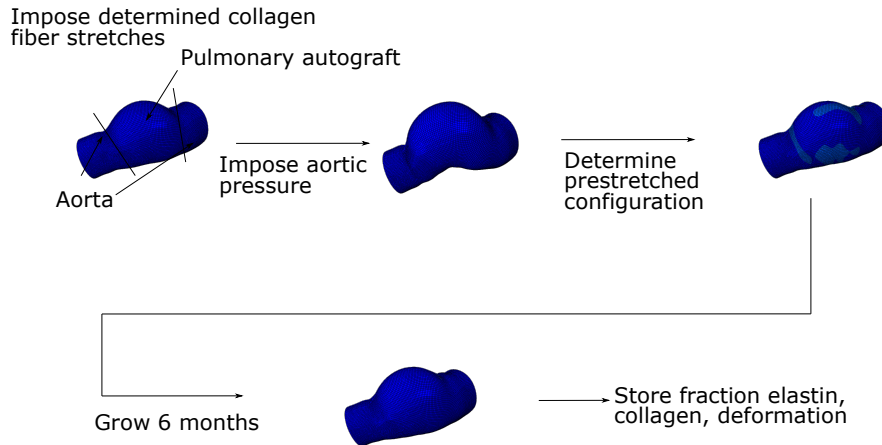


Figure 2: **The different configurations present in the constrained mixture theory.** Each constituent α has its own stress-free configuration at time of deposition τ . The tensor that expresses the deformation the constituent undergoes from its own stress-free configuration to the configuration it has in the body is referred to as a deposition stretch tensor. The deposition stretch tensor of that constituent $\mathbf{G}^{\alpha}(\tau)$ maps this stress-free configuration to the intermediate configuration at the current time τ . The deformation gradients $\mathbf{F}(\tau)$ and $\mathbf{F}(s)$ express the deformation that the body undergoes from time point 0 to time point τ , respectively s .

Figure 3
Simulation 1 Pulmonary artery under aortic pressure



Simulation 2 Pulmonary autograft under aortic pressure



Simulation 3 Biaxial tests of relevant tissues

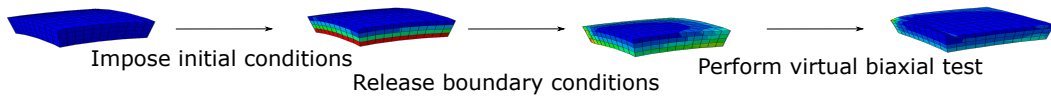


Figure 3: **The workflow for the different virtual experiments.** The workflow to virtually repeat the experiments consists of three separate simulations. First, an ideal cylinder simulates the homeostatic conditions for the pulmonary artery. This ideal cylinder is then brought to aortic pressure and allowed to grow. The second simulation uses the sheep specific geometry to simulate the growth processes in the pulmonary autograft using either CMT or KG models. The third type of simulation is done for CMT models and consists of virtual biaxial experiments.

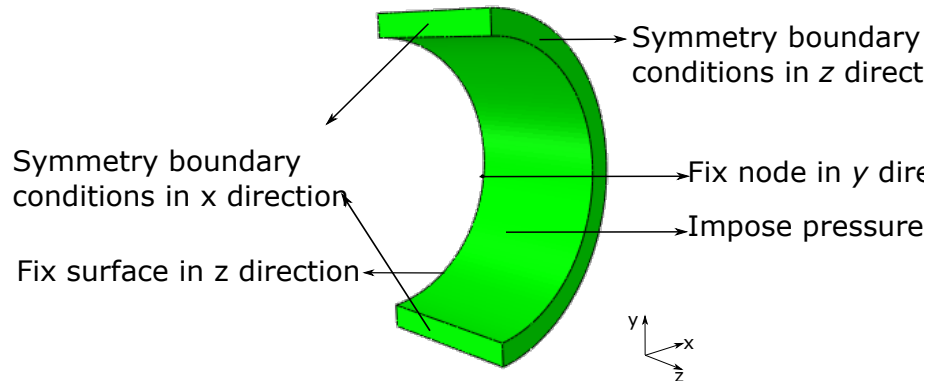
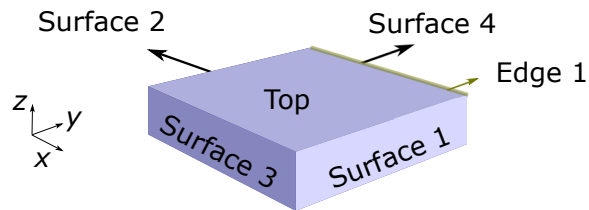
Figure 4

Figure 4: **The boundary and loading conditions for the ideal cylinder.** To simulate the loading in an ideal cylinder, symmetry boundary conditions are used.

Figure 5

Step 1: Fix all nodes in all directions.

Step 2: Fix top surface in z, surface 1 and 2 in x and surface 3 and in y.

Step 3: Fix edge 1 in z, displace surface 1 and 2 in x and surface 3 and 4 in y.

Figure 5: **The boundary conditions for the virtual biaxial test.** Three steps take place in the simulation of the virtual biaxial test, each with their own boundary conditions.

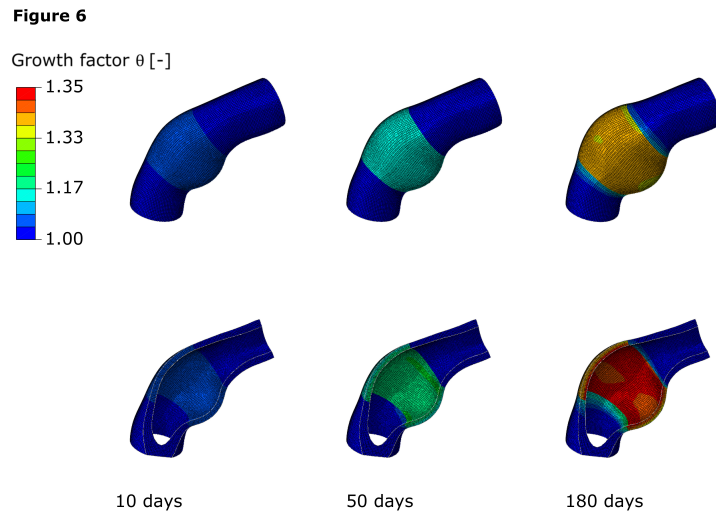


Figure 6: **Growth factor sheep 1 using the kinematic-based growth.** The growth factor increases over time, resulting in an increased diameter. The distribution of the growth factor is rather uniform, but a difference in growth factor through the thickness can be seen. The increase in diameter causes the aorta to expand as well, triggering growth in the adjacent aortic sections.

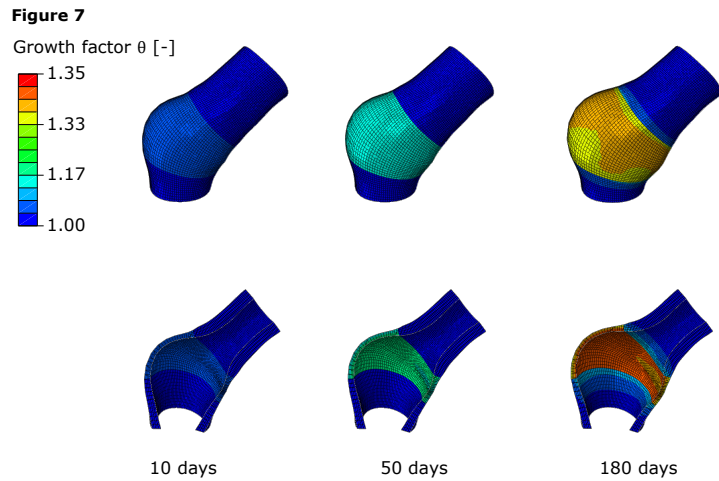


Figure 7: **Growth factor sheep 2 using the kinematic-based growth.** The growth factor increases over time, resulting in an increased diameter. The growth factor changes through the thickness and a heterogeneous distribution of the growth factor is visible. The increase in diameter causes the aorta to expand as well, triggering growth in the adjacent aortic sections.

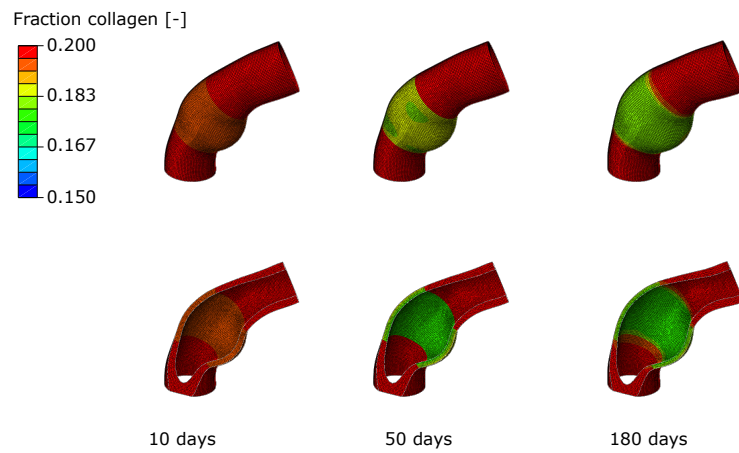
Figure 8

Figure 8: **Collagen fraction over time for sheep 1 using CMT.** After 10 days, collagen is already removed. This removal is more pronounced after 50 days, but becomes more stable at 180 days. Despite the collagen fraction stabilizing after 180 days, the diameter continues to increase. The collagen fraction is not uniformly distributed after 180 days.

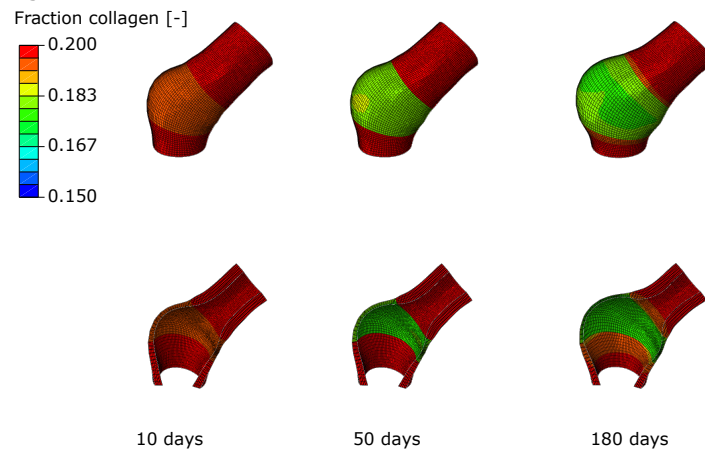
Figure 9

Figure 9: **Collagen fraction over time for sheep 2 using CMT.** After 10 days, collagen is already removed. This removal is more pronounced after 50 days, but becomes more stable at 180 days. Despite the collagen fraction stabilizing after 180 days, the diameter continues to increase. The increase in diameter causes the aorta to expand, triggering growth and resulting in a decrease in collagen fraction in the adjacent aortic section.

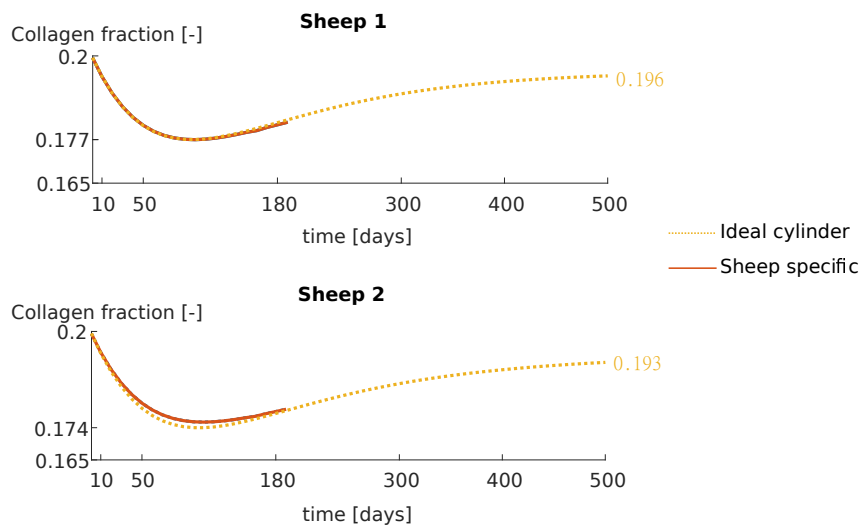
Figure 10

Figure 10: **Average collagen fraction in pulmonary autograft.** An initial decrease in collagen fraction is followed by an increase. The collagen fraction in the ideal cylinder appears to stabilize at a different value than the initial value of 0.2.

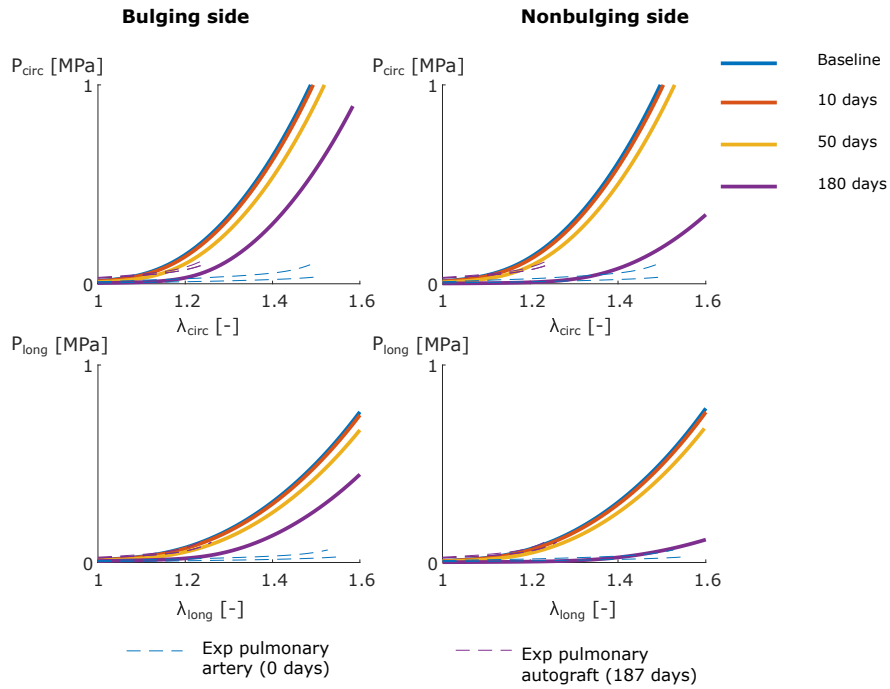
Figure 11

Figure 11: **The virtual stress-stretch curves of the sample on the bulging and nonbulging part of the autograft of sheep 1.** The first Piola-Kirchhoff stress is plotted with respect to the stretch. The dashed lines give the experimental curves of sheep 1 for the pulmonary artery samples (2) and pulmonary autograft samples (2). Each dashed curve corresponds to one sample. The virtual stress-stretch curves show a delayed stiffening effect. This delay is more pronounced for the sample on the nonbulging side.

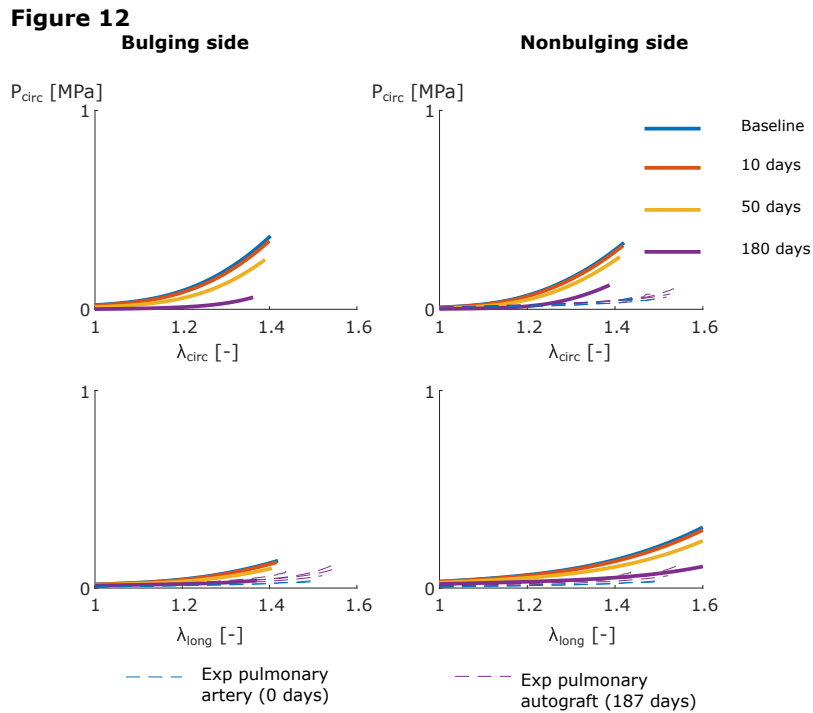


Figure 12: **The virtual stress-stretch curves of the sample on the bulging and nonbulging part of the autograft of sheep 2.** The first Piola-Kirchhoff stress is plotted with respect to the stretch. The dashed lines give the experimental curves of sheep 2 for the pulmonary artery samples (2) and pulmonary autograft samples (2). Each dashed curve corresponds to one sample. The virtual stress-stretch curves show a delayed stiffening effect. This delay is more pronounced for the sample on the bulging side.

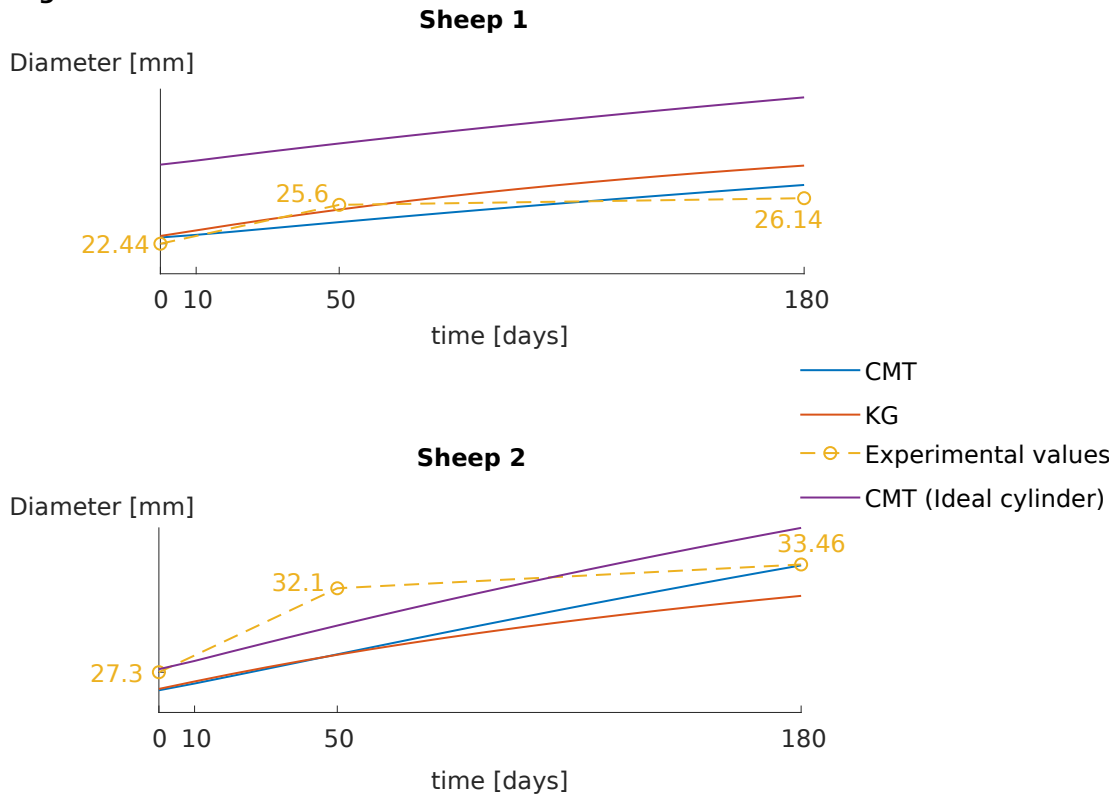
Figure 13

Figure 13: **Measured diameter over time.** The diameter increases for both sheep. The experimental data shows an initial steep increase followed by a lower increase, but the constrained mixture theory (CMT) and kinematic growth (KG) models show a more linear increase.

Figure 14

Average collagen stretch [-]

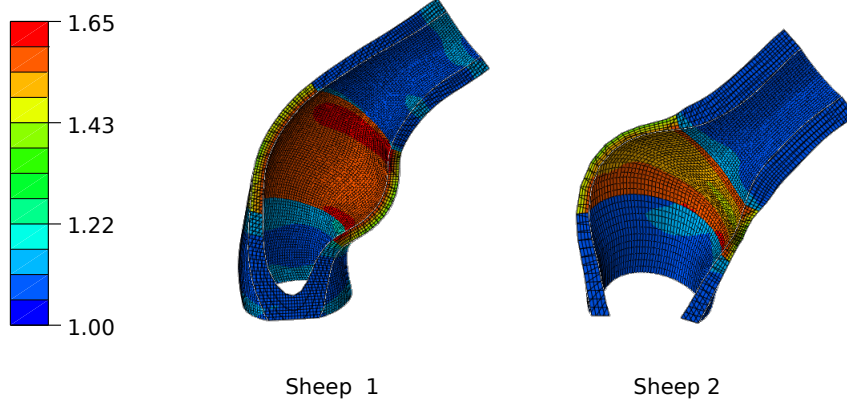


Figure 14: **Average collagen stretch.** The average stretch the collagen fibers feel is different in both geometries, with a less uniform distribution in sheep 2 as it is more asymmetric.

6 Appendix

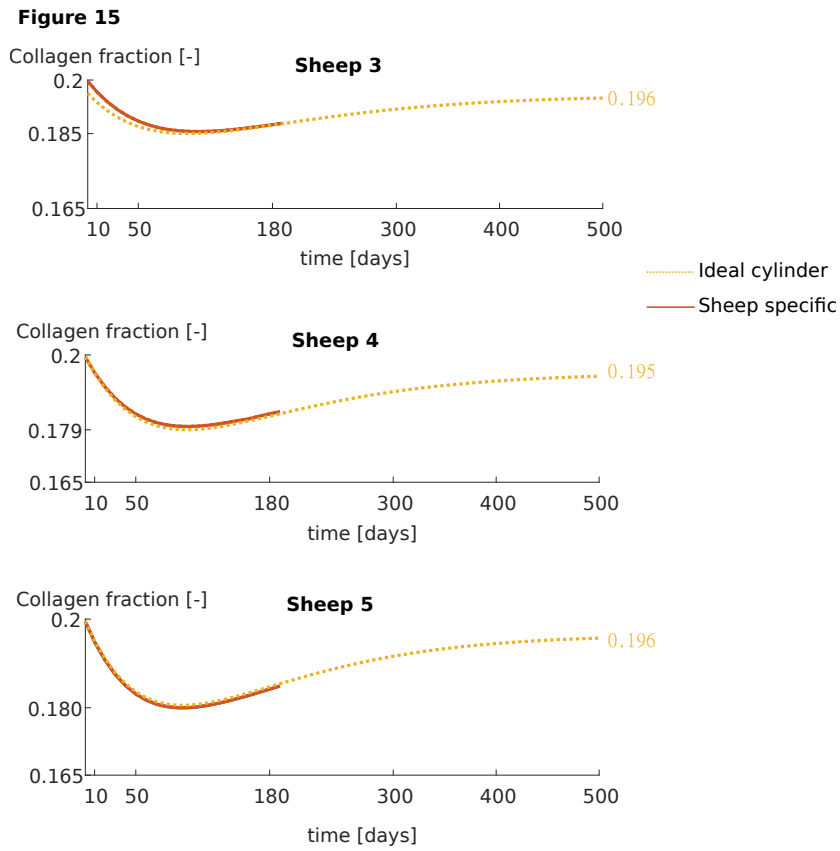


Figure 15: **Average collagen fraction in pulmonary autograft.** An initial decrease in collagen fraction is followed by an increase. The collagen fraction in the ideal cylinder appears to stabilize at a different value than the initial value of 0.2.

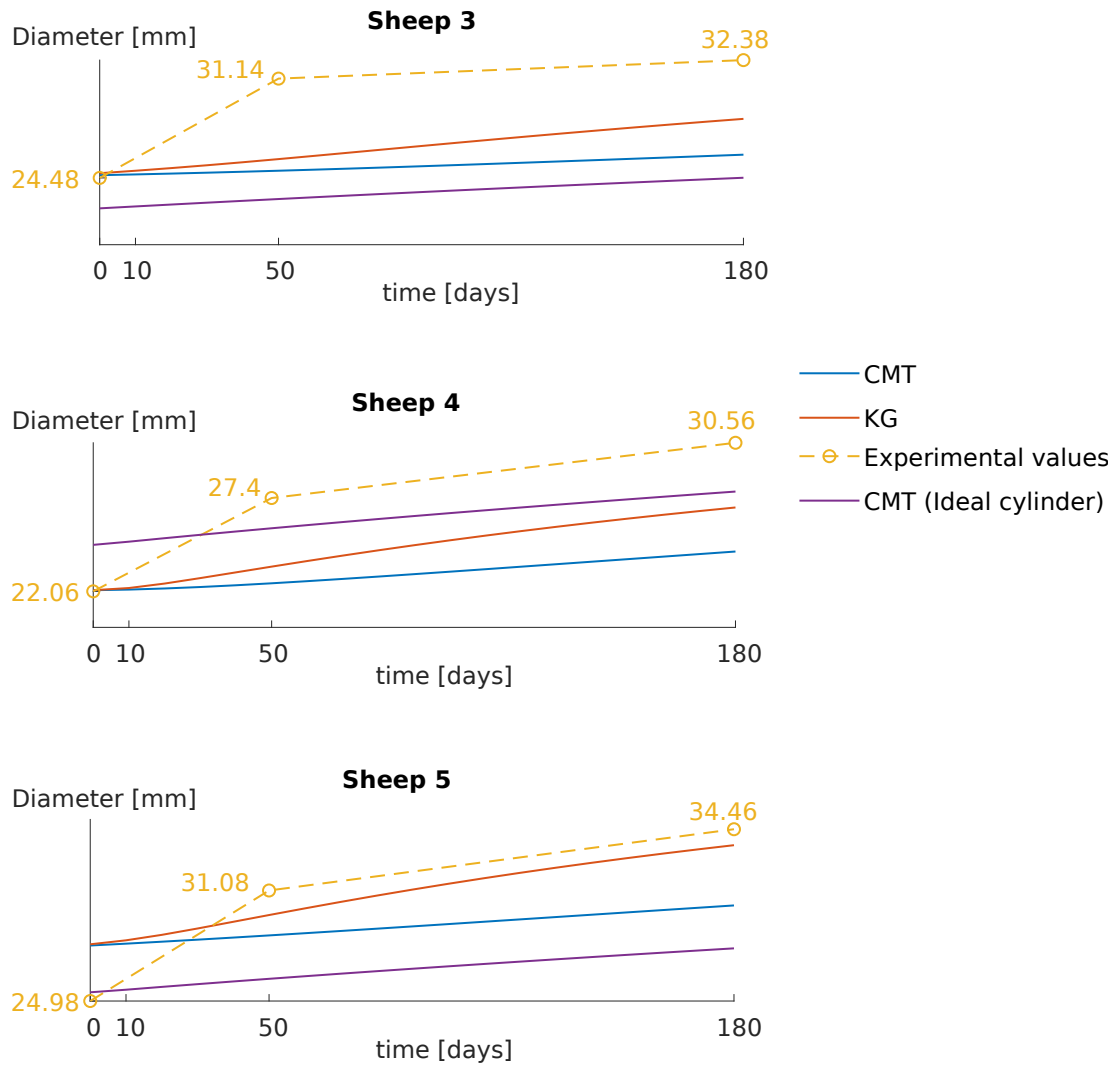
Figure 16

Figure 16: **Measured diameter over time.** The diameter increases for all sheep. The experimental data shows an initial step increase followed by a lower increase, but the constrained mixture theory (CMT) and kinematic growth (KG) models show a more linear increase.

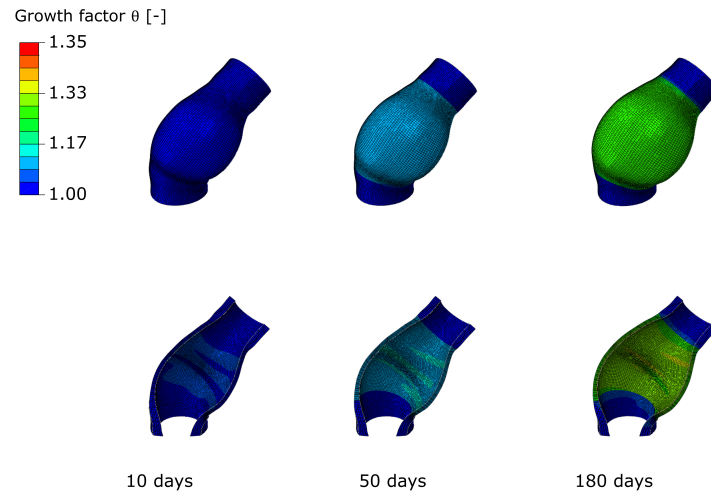
Figure 17

Figure 17: **Growth factor sheep 3 using the kinematic-based growth.** The growth factor increases over time, resulting in an increased diameter. The growth factor changes through the thickness and a heterogeneous distribution of the growth factor is visible. The increase in diameter causes the aorta to expand as well, triggering growth in the adjacent aortic sections.

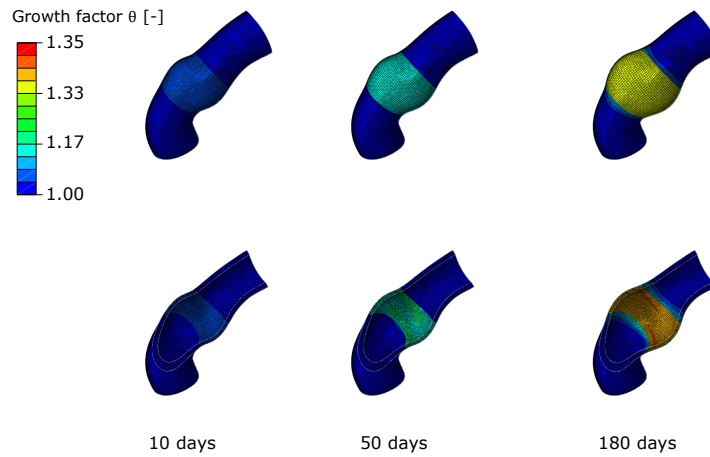
Figure 18

Figure 18: **Growth factor sheep 4 using the kinematic-based growth.** The growth factor increases over time, resulting in an increased diameter. The growth factor changes through the thickness and a heterogeneous distribution of the growth factor is visible. The increase in diameter causes the aorta to expand as well, triggering growth in the adjacent aortic sections.

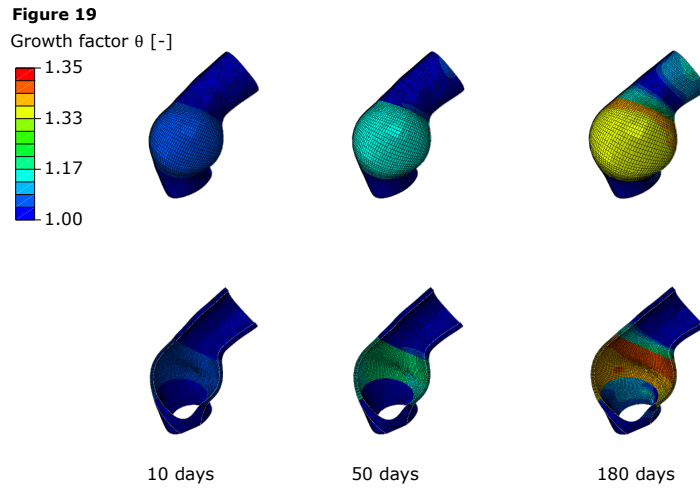


Figure 19: **Growth factor sheep 5 using the kinematic-based growth.** The growth factor increases over time, resulting in an increased diameter. The growth factor changes through the thickness and a heterogeneous distribution of the growth factor is visible. The increase in diameter causes the aorta to expand as well, triggering growth in the adjacent aortic sections.

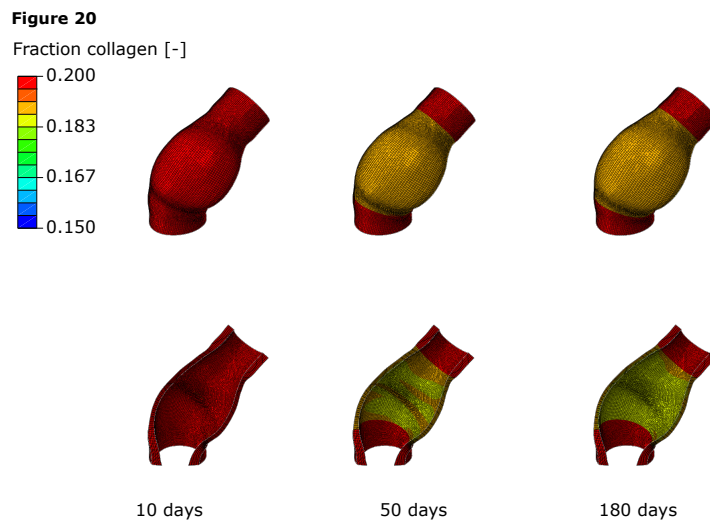


Figure 20: **Collagen fraction over time for sheep 3 using CMT.** After 10 days, collagen is already removed. This removal is more pronounced after 50 days, but becomes more stable at 180 days. Despite the collagen fraction stabilizing after 180 days, the diameter continues to increase. The collagen fraction is not uniformly distributed after 180 days.

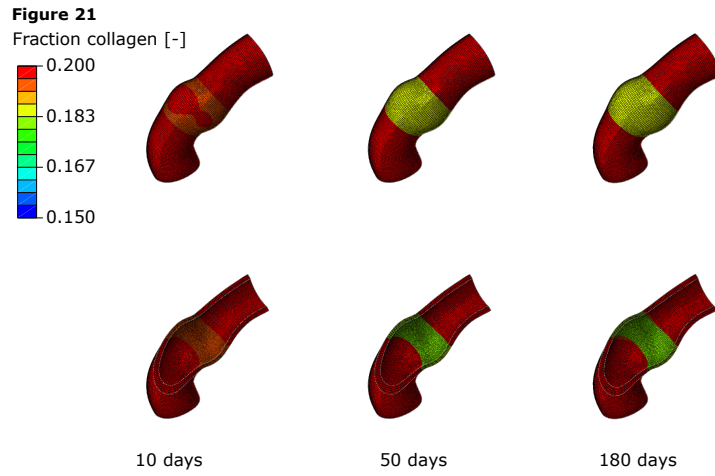


Figure 21: **Collagen fraction over time for sheep 4 using CMT.** After 10 days, collagen is already removed. This removal is more pronounced after 50 days, but becomes more stable at 180 days. Despite the collagen fraction stabilizing after 180 days, the diameter continues to increase. The collagen fraction is not uniformly distributed after 180 days.

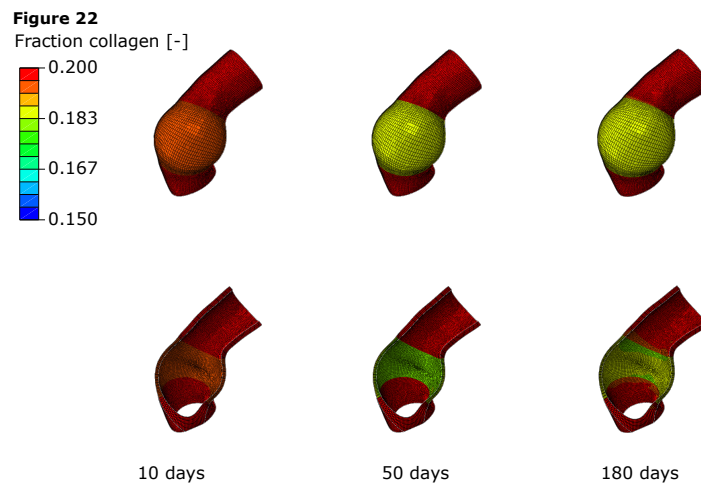
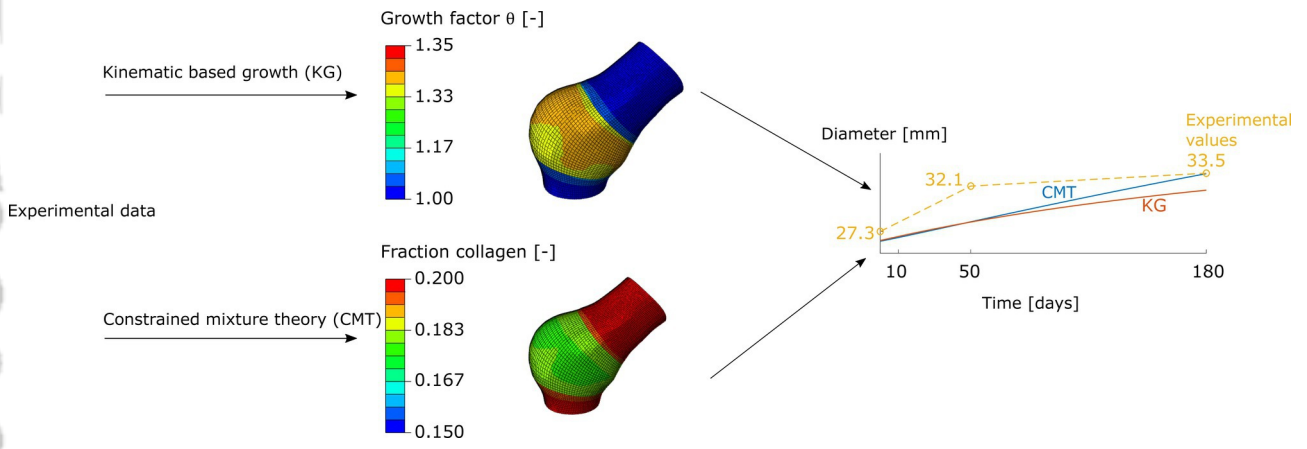


Figure 22: **Collagen fraction over time for sheep 5 using CMT.** After 10 days, collagen is already removed. This removal is more pronounced after 50 days, but becomes more stable at 180 days. Despite the collagen fraction stabilizing after 180 days, the diameter continues to increase. The collagen fraction is not uniformly distributed after 180 days.

Growth and remodeling in the pulmonary autograft: computational evaluation using kinematic growth models and constrained mixture theory

by Julie Vastmans*, Lauranne Maes, Mathias Peirlinck, Emma Vanderveken, Filip Rega, Ellen Kuhl, Nele Famaey.

Within this work, the two main types of growth and remodelling models, kinematic based growth and growth based on constrained mixture theory, are compared by applying them on the same experimental data. In this experiment, a pulmonary artery was placed in aortic position and its deformation and changing microstructure and mechanical behaviour was tracked over time. Kinematic growth models were capable of describing the changing deformation. Constrained mixture theory was also able to predict changing microstructure and changing mechanical behaviour.



cnm_3545_graphical table of contents.eps